Inorganic Chemistry
Article
pubs.acs.org/IC

Crystal Structures and Photoluminescence across the $La_2Si_2O_7$–$Ho_2Si_2O_7$ System

Alberto J. Fernández-Carrión,[†,‡] Mathieu Allix,[§,∥] Manuel Ocaña,[†] Jorge García-Sevillano,[⊥] Fernando Cusso,[⊥] Andrew N. Fitch,[#] Emmanuelle Suard,[○] and Ana I. Becerro*[,†]

[†]Instituto de Ciencia de Materiales de Sevilla, CSIC-University of Seville, c/Américo Vespucio, 49, 41092 Seville, Spain
[‡]Departamento de Química Inorgánica, Universidad de Sevilla, 41071 Seville, Spain
[§]UPR3079 CEMHTI, CNRS, 1D avenue de la Recherche Scientifique, 45071 Orléans cedex2, France
[∥]Université d'Orléans, Avenue du Parc Floral, BP 6749, 45067 Orléans cedex 2, France
[⊥]Dpto. Física de Materiales C-04, Universidad Autónoma de Madrid, 28049 Madrid, Spain
[#]European Synchrotron Radiation Facility, BP 220, 38043 Grenoble Cedex, France
[○]Institut Laue-Langevin, F-38042 Grenoble 9, France

Supporting Information

ABSTRACT: It is well-known that when an $RE_2Si_2O_7$ matrix is doped with active lanthanide ions, it displays promising luminescent responses for optical applications. The crystalline structure adopted by the silicate matrix as well as the distribution of the dopants among the available RE crystallographic sites have important effects on the luminescent yields of these compounds. The present study is aimed at analyzing the structural behavior as well as the luminescent properties of Ho^{3+}-substituted $La_2Si_2O_7$. Several compositions across the $La_2Si_2O_7$–$Ho_2Si_2O_7$ system were synthesized using the sol–gel method followed by calcination at 1600 °C. The resulting powders were analyzed by means of X-ray and neutron diffraction to determine the phase stabilities across the system. The results indicated a solid solubility region of G-$(La,Ho)_2Si_2O_7$ which extends to the $La_{0.6}Ho_{1.4}Si_2O_7$ composition. Compositions richer in Ho^{3+} show a two-phase domain (G+δ), while δ-$(La,Ho)_2Si_2O_7$ is the stable phase for Ho^{3+} contents higher than 90% ($La_{0.2}Ho_{1.8}Si_2O_7$). Anomalous diffraction data interestingly indicated that the La^{3+} for Ho^{3+} substitution mechanism in the G-$(La,Ho)_2Si_2O_7$ polymorph is not homogeneous, but a preferential occupation of Ho^{3+} for the RE2 site is observed. The Ho^{3+}-doped G-$La_2Si_2O_7$ phosphors exhibited a strong green luminescence after excitation at 446 nm. Lifetime measurements indicated that the optimum phosphor was that with a Ho^{3+} content of 10%.

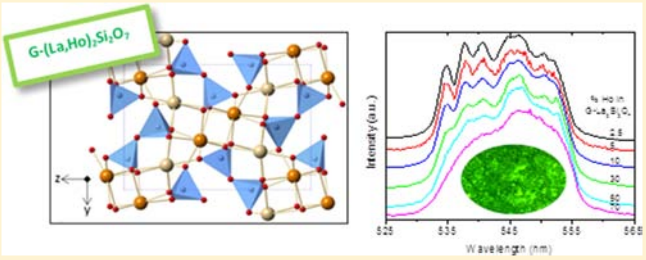

■ INTRODUCTION

Rare-earth pyrosilicates $RE_2Si_2O_7$ ($RE = Ln^{3+}, Sc^{3+}, Y^{3+}$) are well-known for their polymorphism. They exhibit up to seven structure types at normal pressure[1] known as A, B (or α), C (or β), D (or γ), E (or δ), F, and G, which show respectively tetragonal ($P4_1$), triclinic ($P\bar{1}$), monoclinic ($C2/m$), monoclinic ($P2_1/a$), orthorhombic ($Pnam$), triclinic ($P\bar{1}$), and monoclinic ($P2_1/c$) symmetry. Their stability fields were first described by Felsche as a function of the RE^{3+} ionic radius and temperature.[1] Most of the $RE_2Si_2O_7$ compounds are dimorphic with temperature, while a high polymorphism degree is observed for $Sm_2Si_2O_7$, $Eu_2Si_2O_7$, $Ho_2Si_2O_7$, and $Er_2Si_2O_7$. This latter feature may reflect the rather unstable $4f^5$, $4f^6$ and $4f^{10}$, $4f^{11}$ electronic configurations of Sm^{3+}, Eu^{3+} and Ho^{3+}, Er^{3+} cations, respectively. It is interesting to notice that, although Sc^{3+} and Y^{3+} belong to group IIIA of the periodic table, they are frequently grouped with lanthanides under the general name "rare earths", due to their similar physical properties. These similarities are especially significant for Y^{3+}, which exhibits an ionic radius very close to that of Ho^{3+} (0.900 and 0.901 Å, respectively, in VI coordination).[2] In fact, $Y_2Si_2O_7$ shows the same polymorphs as $Ho_2Si_2O_7$: namely, α, β, γ, and δ.[3−6]

Although the structures of individual $RE_2Si_2O_7$ polymorphs are well-known, the studies of crystalline structures adopted by $(RE,RE')_2Si_2O_7$ phases at different temperatures and RE^{3+} contents are rarer and cover only some binary combinations.[7−15] There is clear evidence that the incorporation of rare earths of one type into another type of RE disilicate has a strong influence on the stability of the different polymorphs. It has been suggested that the average RE^{3+} ionic radius may be used empirically to predict phase stability in disilicate solid solutions, on the basis of Felsche's diagram (radius criterion).[14,15] However, it must be noted that this concept is based on evidence from $RE_2Si_2O_7$–$RE'_2Si_2O_7$

Received: July 19, 2013
Published: November 12, 2013

systems whose end members show, at least, one common polymorph. When this is not the case, the radius criterion is not obeyed, as recently demonstrated for the $La_{2-x}Y_xSi_2O_7$ binary system.[10,13] The latter result suggests that the effective ionic radius might not be a unique parameter that has influence over the thermodynamic stability of $(RE,RE')_2Si_2O_7$ polymorphs.

Knowledge of the structural aspects described above is of great importance to understand the behavior and improve the properties of $RE_2Si_2O_7$-based materials. It is well-known that when a $RE_2Si_2O_7$ matrix is doped with active lanthanide ions, it displays promising luminescent responses for applications such as plasma displays, laser materials, and high-energy phosphors.[16−18] Several studies have shown the importance of the crystalline structure adopted by the matrix silicate as well as the distribution of the dopants among the available RE^{3+} crystallographic sites on the luminescent yield of these disilicate compounds.[19−21]

The present study is aimed at analyzing the structural behavior as well as the luminescent properties of the $La_2Si_2O_7$−$Ho_2Si_2O_7$ system. The phase stability across the system will be compared to that recently reported for the $La_2Si_2O_7$−$Y_2Si_2O_7$ system.[13] Given the similarity between the Ho^{3+} and Y^{3+} ionic radii,[2] this study will allow checking the correctness of the radius criterion to determine polymorph stabilities in RE disilicate solid solutions. Were the ionic radius the unique factor influencing the phase stability of $(RE,RE')_2Si_2O_7$ members, the structural behaviors of both systems would be expected to be the same. In a second stage, the luminescent properties of Ho^{3+}-doped $La_2Si_2O_7$ will be analyzed and related to the structural features encountered in the previous section. The choice of $La_2Si_2O_7$ as a matrix for luminescent applications is 2-fold. On the one hand, most of the luminescent studies with $RE_2Si_2O_7$ matrices are based on $Y_2Si_2O_7$[21−23,19,24] and to a lesser extent on $Gd_2Si_2O_7$[25−27] and $Lu_2Si_2O_7$.[28−30] To the best of our knowledge, the use of $La_2Si_2O_7$ as a host matrix is much more scarce and only two studies have been found in the literature, which deal with Tm^{3+}- and Eu^{3+}-doped G-$La_2Si_2O_7$[31,32] (where G refers to the high-temperature modification of $La_2Si_2O_7$[1]). In addition, the use of $La_2Si_2O_7$ for luminescence applications has the advantage of low-cost precursors, in comparison with other matrices such as $Gd_2Si_2O_7$ and $Lu_2Si_2O_7$. Finally, the Ho^{3+} ion has been selected for this study on the basis of its ability to exhibit different transitions in the infrared, visible, and ultraviolet regions, which make it suitable for both down- and upconversion processes.[33] The present work reports for the first time a detailed study of the photoluminescent properties of Ho^{3+}-doped G-$La_2Si_2O_7$ phosphor, including an exhaustive analysis of the La/Ho distribution among the possible crystallographic sites, and reveals that G-$La_2Si_2O_7$ is an efficient host for the luminescence of Ho^{3+} ion.

EXPERIMENTAL SECTION

Synthesis. Different compositions in the $La_2Si_2O_7$−$Ho_2Si_2O_7$ system were synthesized by a sol−gel method using the following precursors: $La(NO_3)_3{\cdot}6H_2O$ (99.99% Aldrich Chemical Co.), $Ho(NO_3)_3{\cdot}5H_2O$ (99.99% Aldrich Chemical Co.), $Si(OC_2H_5)_4$ (TEOS, 99% Aldrich Chemical Co.), and CH_3CH_2OH (ethanol pure, Aldrich Chemical Co.). A TEOS solution in ethanol (1/3 in volume) was added over the appropriate amounts of lanthanum and holmium nitrates previously dissolved in pure ethanol. A slight excess of TEOS (1.1/1 mol % TEOS/$RE(NO_3)_3$) in the initial mixture was necessary to suppress formation of an undesired La−apatite phase. The mixture was stirred at 40 °C until the formation of a pink gel. The gel was then calcined at 60 °C for 24 h in air. Finally, the samples were heated at 500 °C for 2 h using a heating rate of 1 $°C\ min^{-1}$ to remove nitrate. The samples were subsequently annealed at 1600 °C for 80 h. Here and throughout this work, sample compositions will be identified by a LaHo*x* nomenclature, where *x* represents the mole percent of $Ho_2Si_2O_7$ substituted into $La_2Si_2O_7$.

Characterization Techniques. *X-ray Powder Diffraction (XRPD).* XRPD data were measured on a PANalytical X'Pert Pro diffractometer (Cu $K\alpha$) with an X-Celerator detector over an angular range of $10° < 2\theta < 130°$ and a 2θ step width of 0.016°. The ICDD powder diffraction database[34] was used to identify the crystalline phases in the powder patterns.

Neutron Powder Diffraction (NPD). NPD experiments were carried out on the D2B high-resolution/high-flux powder diffractometer at the Institut Laüe-Langevin in Grenoble, France. The samples were packed in vanadium cans. Data were acquired with a λ 1.594 Å at 2θ intervals of 0.05° over the $10° < 2\theta < 160°$ angular range.

Combined Neutron and X-ray Rietveld Refinements. These refinements[35] were carried out using the JANA2006 software[36] to obtain unit cell parameters as well as to check that all sites were fully occupied (no vacancies) and no special ordering or supplementary crystallographic positions were present in the studied structures. Refined parameters were as follows: background coefficients, zero error, scale factors, unit cell parameters, anisotropic atomic displacement parameters, atomic positions, and site occupation factors.

Anomalous High-Resolution Synchrotron Powder Diffraction (ASD). ASD was used to help differentiate La from Ho in the 5, 10, 30, 50, and 70% Ho^{3+}-doped G-$La_2Si_2O_7$ samples. Data were measured on the ID31 diffractometer at the European Synchrotron Radiation Facility (ESRF) over the 2θ range 0−35° in a continuous-scanning mode, sampling the data every 0.0005°. Data from the nine counters were combined, normalized, and rebinned to a step of 0.002° using the standard routines available on the instrument.[37] Measurements were made at room temperature using wavelengths of λ 0.3542, 0.3187, and 0.3185 Å. The samples were contained in 0.4 mm diameter borosilicate glass capillaries spun at 50 Hz during data collection. The patterns were analyzed using the Rietveld method[35] with the JANA2006 software.[36] Refined parameters were as follows: background coefficients, zero error, scale factors, unit cell parameters, anisotropic atomic displacement parameters, atomic positions, and La/Ho occupancies.

Luminescence Measurements. The excitation and emission spectra of the powder phosphors were recorded in a Horiba Jobin-Yvon Fluorolog3 spectrofluorometer operating in the front face mode. The CIE color coordinates of the emitted light were calculated from the emission spectra, considering a 2° observer. Fluorescence dynamics has been investigated under 532 nm excitation, corresponding to the second harmonics of a Nd:YAG pulsed laser (SpectraPhysics DCR 2/2A 3378) with a 10 ns pulse width and 10 Hz repetition rate. The luminescence was dispersed with a Princeton Instruments monochromator (Acton SP2500) and detected with a Thorn Emi QB9558 photomultiplier in the visible range and an InGaAs Judson G5883 photodiode in the infrared region. The transient luminescence signals were amplified and then recorded with a Tektronix TDS 420 digital oscilloscope.

RESULTS

Structural Characterization of the $La_2Si_2O_7$−$Ho_2Si_2O_7$ System. In the following sections, we first report the results corresponding to the analysis of the different phases encountered across the $La_2Si_2O_7$−$Ho_2Si_2O_7$ system calcined at 1600 °C as well as the transition compositions. Second, a detailed structural analysis of each phase encountered is described, with emphasis on the La/Ho distribution between the two different RE crystallographic sites of the G-$(La,Ho)_2Si_2O_7$ unit cell.

Phase Evolution across the $La_2Si_2O_7$−$Ho_2Si_2O_7$ System. Figure 1 shows the conventional X-ray powder diffraction (XRPD) patterns of representative compositions of the $La_2Si_2O_7$−$Ho_2Si_2O_7$ system calcined at 1600 °C. The LaHo0 pattern matches the standard pattern of pure G-$La_2Si_2O_7$ (monoclinic symmetry, PDF 01-082-0729). Increasing Ho^{3+} content leads to a shift of the reflections to higher 2θ values

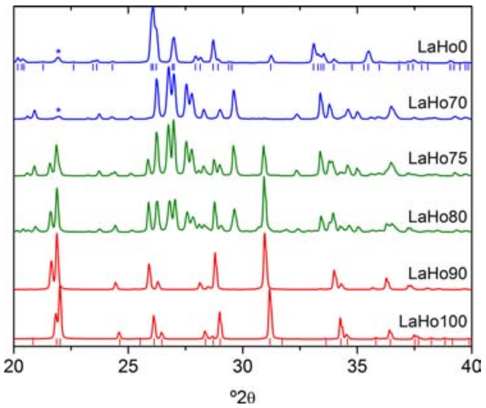

Figure 1. X-ray powder diffraction (XRPD) patterns of representative compositions of the $La_2Si_2O_7$−$Ho_2Si_2O_7$ system calcined at 1600 °C. Asterisks correspond to cristobalite. The tick marks at the top correspond to G-$La_2Si_2O_7$ (ICDD PDF 01-082-0729), while those at the bottom correspond to δ-$Ho_2Si_2O_7$ (ICDD PDF 04-007-4854).

(smaller *d* spacings) as a consequence of the smaller ionic radius of Ho^{3+} in comparison to La^{3+} (1.015 and 1.160 Å, respectively, in VIII coordination).[2] The shifts are not the same for all reflections, and this fact allows the observation of more resolved peaks as the Ho content increases. For example, the three reflections under the band at ∼26° 2θ in the LaHo0 pattern are clearly resolved into three peaks at 26.4, 26.9, and 27.1° 2θ in the LaHo70 pattern. This fact is a consequence of the anisotropic variations of lattice parameters, which will be analyzed in the next subsection. The LaHo75 XRPD pattern shows, in addition to the G reflections, a number of new reflections that match those reported for δ-$Ho_2Si_2O_7$ (orthorhombic symmetry, PDF 04-007-4854),[6] with slight differences in peak positions due to the presence of La^{3+} in the δ-$Ho_2Si_2O_7$ structure. Therefore, the compositional limit between the G and G+δ stability fields is found between the LaHo70 and LaHo75 compositions. The simultaneous presence of δ- and G-$(La,Ho)_2Si_2O_7$ reflections is observed in all patterns of the LaHo75−LaHo85 compositional range, the δ/G ratio increasing with increasing Ho^{3+} content. Finally, the LaHo90 pattern shows, exclusively, reflections corresponding to δ-$Ho_2Si_2O_7$, with progressive changes in the positions of the reflections, as expected from the substitution of La^{3+} for Ho^{3+} in the δ-$Ho_2Si_2O_7$ structure. Therefore, the compositional limit in this case was found between the LaHo85 and LaHo90 compositions. A comparison of the phase stability regions of the $La_2Si_2O_7$−$Ho_2Si_2O_7$ system at 1600 °C with those of the analogous $La_2Si_2O_7$−$Y_2Si_2O_7$ system[13] at the same temperature shows a significant change in the compositional limit corresponding to the G → G+δ transition (between 70% and 75% for the LaHo system in comparison to 59% for the LaY system), while the G+δ → δ transition shows very similar transition compositions in both systems (between 85% and 90% for the LaHo system and 86% for the LaY system). Therefore, the G-$La_2Si_2O_7$ phase seems able to host more Ho^{3+} than Y^{3+} in its structure. Given the similarity between the ionic radii of Ho^{3+} and Y^{3+} (1.015 and 1.019 Å, respectively, in VIII coordination),[2] this different behavior cannot be explained in terms of ionic radius of the substituting atoms. It is very likely therefore that the electronic structure of the substituting atoms plays an important role in the extension of the solid solution.

The unit cell parameters of the G- and δ-$(La,Ho)_2Si_2O_7$ phases have been determined using combined neutron and X-ray Rietveld refinements.[35] Starting structural parameters have been taken from those reported for G-$La_2Si_2O_7$ and δ-$Ho_2Si_2O_7$.[6] Table 1 shows the unit cell parameters for the G- and δ-$(La,Ho)_2Si_2O_7$ phases over the whole compositional range. It can be observed that while the *b* and *c* cell parameters of the G phase (compositional range 0−70% Ho^{3+}) decrease considerably with composition, the corresponding variation of the *a* value is very small. This fact explains the apparent progressive splitting of the peaks in the XRPD patterns of the LaHo0-LaHo70 compositions (Figure 1), as noted above. On the other hand, the behavior of the G-$(La,Ho)_2Si_2O_7$ unit cell volume (Figure 2) shows two different stages: it decreases linearly with increasing Ho^{3+} content from LaHo0 to LaHo70 and stays constant from LaHo70 to LaHo85. On the other hand, the δ-$(Ho,La)_2Si_2O_7$ unit cell volume remains constant in the LaHo75−LaHo90 compositional range and decreases with increasing Ho^{3+} content from LaHo90 to LaHo100. The fact that the unit cell volume remains constant over a specific compositional range is a clear indication of the saturation of both phases in La^{3+} and Ho^{3+} (La/Ho ratio remains fixed in each phase) and, therefore, of the coexistence of both phases in such a range. This is possible because the G/δ ratio is changing with composition. The linear behavior, on the other hand, indicates that $Ho_2Si_2O_7$ is completely soluble in G-$La_2Si_2O_7$ from LaHo0 up to LaHo70 and that $La_2Si_2O_7$ is soluble in δ-$Ho_2Si_2O_7$ from LaHo90 to LaHo100.

Table 1. Unit Cell Parameters for the G- and δ-$(La,Ho)_2Si_2O_7$ Phases from Combined Neutron and X-ray Rietveld Refinements[a]

% of Ho^{3+}	*a* (Å)	*b* (Å)	*c* (Å)	β (deg)	*V* (Å^3)
G Phase					
10	5.41202(5)	8.76170(8)	14.2216(1)	112.6512(6)	622.35(1)
30	5.40397(5)	8.69484(7)	14.0823(2)	112.489(1)	611.365(8)
50	5.38338(7)	8.6081(1)	13.9307(2)	112.147(1)	597.93(2)
70	5.36262(8)	8.4933(1)	13.7865(2)	111.269(1)	585.16(2)
75	5.3626(1)	8.4916(2)	13.7825(3)	111.275(2)	584.75(3)
80	5.3596(1)	8.4859(2)	13.7825(3)	111.194(2)	584.07(3)
85	5.357(1)	8.4767(8)	13.811(2)	111.20(1)	584.77(8)
δ Phase					
75	13.7609(3)	5.0274(1)	8.2244(2)		568.98(3)
80	13.7611(2)	5.02977(9)	8.2240(1)		569.23(4)
85	13.7651(6)	5.0314(2)	8.2238(3)		569.57(6)
90	13.7523(1)	5.0328(4)	8.21361(7)		568.48(1)
100	13.6754(5)	5.0226(2)	8.1594(3)		560.44(3)

[a] The space group is $P2_1/c$ for the G phase and *Pnam* for the δ phase.

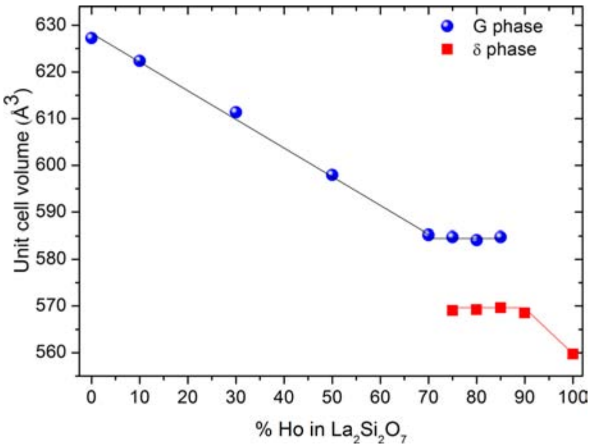

Figure 2. G- and δ-$(La,Ho)_2Si_2O_7$ unit cell volume values. The error bars are within the size of the symbol.

Crystal Structure and Substitution Mechanism of La^{3+} and Ho^{3+} in the G-$(La,Ho)_2Si_2O_7$ Compositions. The G-$La_2Si_2O_7$ unit cell contains two different La crystallographic sites (RE1 and RE2), both of which exhibit 8-fold coordination.[1] We performed combined neutron and X-ray diffraction measurements and found that all sites were fully occupied (no vacancies) and no special ordering or supplementary crystallographic positions were apparent. Unfortunately, the rather similar neutron scattering lengths of La and Ho (8.24 and 8.01 fm, respectively) and their close X-ray scattering factors did not allow definition of the La^{3+} and Ho^{3+} occupancies on both RE sites. In order to analyze precisely the substitution mechanism of La^{3+} and Ho^{3+} on both crystallographic sites, anomalous synchrotron powder diffraction (ASD) patterns were then recorded on several compositions of the G-$(La,Ho)_2Si_2O_7$ solid solution. The structural refinements of the ASD data for LaHo5, LaHo10, LaHo30, LaHo50, and LaHo70 have been performed using the single G phase with space group $P2_1/c$ and starting parameters for G-$La_2Si_2O_7$ from Christensen.[6] Figure 3a shows, as an example, the experimental and fitted patterns for LaHo50 (G-$La_{1.0}Ho_{1.0}Si_2O_7$) recorded at λ 0.3185 Å. Tables 2 and 3 contain the refined atomic parameters with site occupation factors for RE1 and RE2, as well as main distances and angles. These data have been used to represent the structure of the G-$La_{1.0}Ho_{1.0}Si_2O_7$ phase (Figure 3b). The structure consists of columns containing eclipsed double-tetrahedra Si_2O_7 groups, packed with their backbones toward each other but at alternating heights of $a/2$. Both lanthanide sites are in 8-fold oxygen coordination. The anomalous diffraction data clearly evidenced that Ho much prefers to occupy site RE2. This behavior was also observed in the other compositions analyzed, as shown in Figure 4, which displays the behavior of the Ho occupation of the RE1 and RE2 sites versus the nominal Ho content. Therefore, the La^{3+} for Ho^{3+} substitution mechanism in the G polymorph does not obey a homogeneous distribution evolution. The preference of Ho^{3+} (of smaller ionic radius than La^{3+})[2] to occupy the RE2 site can be explained by the fact that, in the $La_2Si_2O_7$ end member, the $RE2O_8$ polyhedron is smaller than the $RE1O_8$ group (and, correspondingly, the RE2−O distances are shorter than the RE1−O distances). The substitution of the RE1 site for Ho^{3+} is thus unfavorable. In this sense, the G-$(La,Ho)_2Si_2O_7$ solid solution shows a behavior very similar to that observed in G-$(La,Y)_2Si_2O_7$, where the RE1 site becomes Y-substituted only when the RE2 site is nearly fully Y-substituted (around the LaY50 composition).[13]

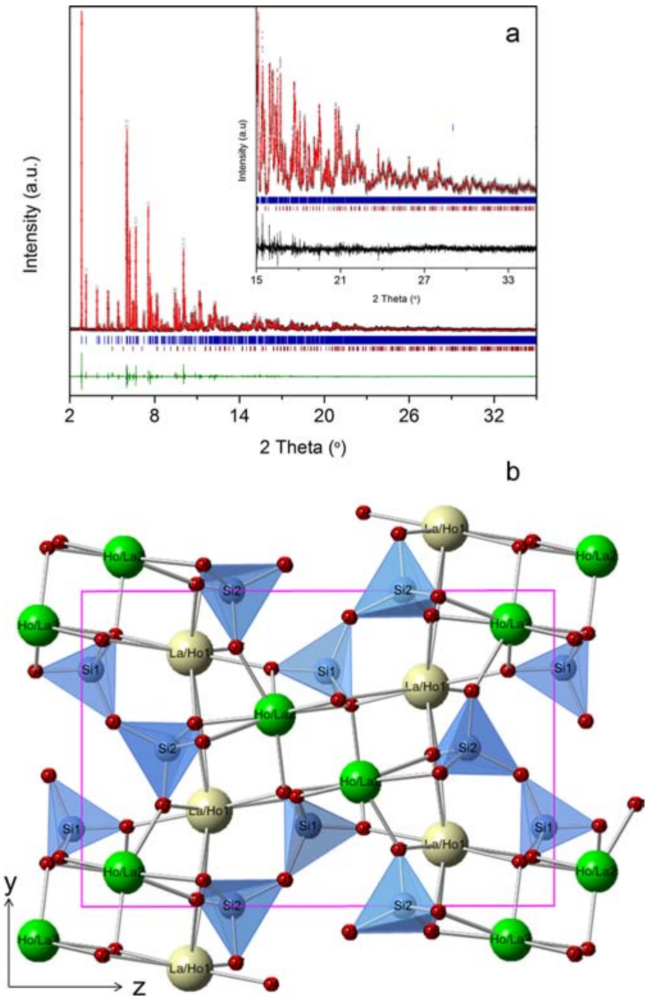

Figure 3. (a) Experimental (circles) and fitted (solid line) anomalous X-ray diffraction pattern (λ 0.3185 Å) of G-$La_{1.0}Ho_{1.0}Si_2O_7$ (LaHo50). The difference curve is also shown. The indexing is the G phase. Inset: magnification of the 15−35° 2θ region. (b) View of the G-$La_{1.0}Ho_{1.0}Si_2O_7$ refined structure along the [100] direction.

Crystal Structure of δ-$La_{0.2}Ho_{1.8}Si_2O_7$. The following details the crystal structure refinement of δ-$La_{0.2}Ho_{1.8}Si_2O_7$, which is the δ-$RE_2Si_2O_7$ structure with the highest La composition. Two similar crystallographic descriptions for the δ-$RE_2Si_2O_7$ structure can be found in the literature: Smolin[38] described the structure of δ-$Gd_2Si_2O_7$ considering two different RE crystallographic sites and using space group $Pna2_1$, while Dias et al.[39] described the δ-$Y_2Si_2O_7$ structure using the space group $Pnam$ with a unique crystallographic site for the RE. The existence of a unique Y^{3+} crystallographic site in δ-$Y_2Si_2O_7$ was confirmed later through ^{89}Y NMR studies,[40] and we have therefore preferred the latter description to refine the crystal structure of δ-$La_{0.2}Ho_{1.8}Si_2O_7$. Because there is only one RE site in the $Pnam$ description, no specific long-range La/Ho substitution mechanism can take place. Therefore, anomalous diffraction was not necessary in this case and combined X-ray and neutron diffraction were used instead. The relative occupancies of the single RE site by La and Ho were fixed in agreement with the corresponding nominal composition. Anisotropic thermal parameters have been considered for the single RE site. Figure 5a shows the experimental and fitted neutron diffraction patterns, while Tables 4 and 5 show the related refined atomic parameters and

Table 2. Refined Atomic Coordinates for G-$La_{1.0}Ho_{1.0}Si_2O_7$ (LaHo50) Calcined at 1600 °C from ASD Data Collected at Room Temperature[a]

atom	site	x	y	z	U_{iso} (×100) (Å^2)	occ
La1/Ho1	4e	0.51426(9)	0.80505(5)	0.77054(4)	0.83(1)	0.804(2)/0.196(2)
La2/Ho2	4e	0.82223(8)	0.60693(4)	0.59044(3)	0.63(1)	0.196(2)/0.804(2)
Si1	4e	0.7468(4)	0.2475(2)	0.0218(2)	1.07(6)	1
Si2	4e	0.9541(4)	0.5001(2)	0.1825(2)	0.85(5)	1
O1	4e	0.7935(8)	0.4169(5)	0.0711(3)	1.4(1)	1
O2	4e	0.0332(8)	0.1589(5)	0.0434(3)	1.4(1)	1
O3	4e	0.5783(8)	0.1348(5)	0.0735(3)	0.7(1)	1
O4	4e	0.5482(7)	0.2543(4)	−0.0960(3)	0.6(1)	1
O5	4e	0.7908(8)	0.4779(5)	0.2560(3)	1.1(1)	1
O6	4e	0.2385(8)	0.4219(5)	0.2423(3)	0.9(1)	1
O7	4e	0.0304(7)	0.6837(5)	0.1699(3)	1.2(1)	1

[a] Crystal data: space group $P2_1/c$, a = 5.38354(2) Å, b = 8.61038(5) Å, c = 13.92948(8) Å, β = 112.1389(2)°, R_{wp} = 7.81%, R_p= 5.86%, χ^2 = 0.87.

Table 3. Main Atomic Distances and Angles for G-$La_{1.0}Ho_{1.0}Si_2O_7$ (LaHo50) Calcined at 1600 °C from ASD Data Collected at Room Temperature

La1/Ho1−O distance (Å)		La2/Ho2−O distance (Å)		Si−O distance (Å)	
La1/Ho1−O2	2.827(4)	La2/Ho2−O2	2.318(5)	Si−O1	1.592(5)
La1/Ho1−O3	2.460(5)	La2/Ho2−O2	2.740(5)	Si−O2	1.645(5)
La1/Ho1−O4	2.366(4)	La2/Ho2−O3	2.492(3)	Si−O3	1.666(5)
La1/Ho1−O5	2.883(5)	La2/Ho2−O3	2.425(4)	Si−O4	1.586(4)
La1/Ho1−O5	2.445(5)	La2/Ho2−O4	2.390(4)	Si−O5	1.630(4)
La1/Ho1−O6	2.409(5)	La2/Ho2−O5	2.468(4)	Si−O6	1.592(6)
La1/Ho1−O6	2.729(4)	La2/Ho2−O6	2.484(5)	Si−O7	1.590(4)
La1/Ho1−O7	2.451(4)	La2/Ho2−O7	2.190(4)	Si−O8	1.660(5)
Si−O Angles (deg)					
O4−Si1−O1	110.3	O6−Si2−O5	105.6		
O4−Si1−O2	115.3	O6−Si2−O1	111.9		
O4−Si1−O3	101.8	O6−Si2−O7	103.3		
O1−Si1−O2	111.3	O5−Si2−O1	109.6		
O1−Si1−O3	111.7	O5−Si2−O7	113.7		
O2−Si1−O3	106.0	O1−Si1−O7	112.4		
Si1−O1−Si2 139.0					

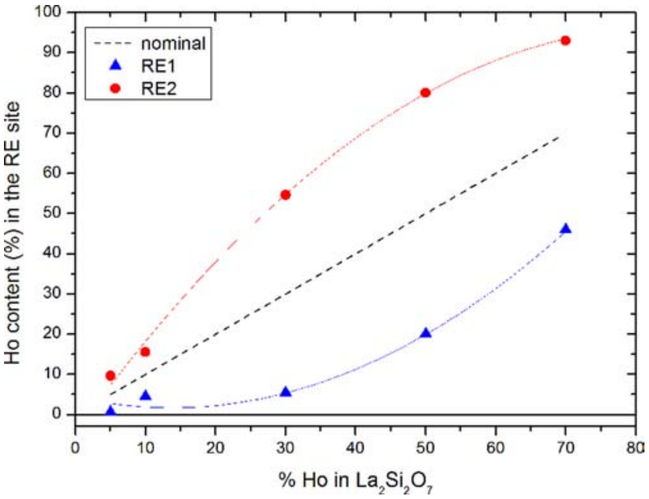

Figure 4. Ho^{3+} content of the two RE sites vs the nominal Ho^{3+} substitution content in the G phase.

main distances and angles. These data have been used to represent the structure of the δ phase, showing RE thermal ellipsoids drawn at the 99% probability level (Figure 5b). As small thermal parameters with no specific anisotropy were observed on the unique RE site, the use of the $Pnam$ structural model appears correct (high thermal parameters with especially a strong anisotropy along the z axis would have led us to reconsider the $Pna2_1$ space group instead). The structure consists of isolated Si_2O_7 double-tetrahedra groups with 157.2° for the Si1−O3−Si2 angle and 7-fold coordination for the RE. It is interesting to note that the double-tetrahedra groups show a distinct difference between the lengths of the terminal oxygens to the Si atoms (mean Si−O_t distance 1.610(6) Å) and that of the bridging oxygen to the Si atom (mean Si−O_{br} distance 1.671(16) Å). These values are very similar to those reported for δ-$La_{0.2}Y_{1.8}Si_2O_7$ (mean Si−O_t distance 1.609(6) Å, mean Si−O_{br} distance 1.670(5) Å).[13]

Luminescent Properties of Ho^{3+}-Doped G-$La_2Si_2O_7$. The energy levels of Ho^{3+} and the relevant optical transitions are summarized in Figure 6a. Figure 7a shows the excitation spectrum of the 2.5% Ho-doped G-$La_2Si_2O_7$ sample monitored at the characteristic $^5F_4$:$^5S_2$ → $^5I_8$ emission of Ho^{3+} at 550 nm. Several sharp peaks can be observed in the spectrum, corresponding to f−f transitions of the Ho^{3+} ion, with maxima at 360 nm ($^5I_8$ → $^3H_6$:$^5G_5$), 417 nm ($^5I_8$ → $^3G_5$), and 446 nm ($^5I_8$ → $^5G_6$: $^5F_1$).

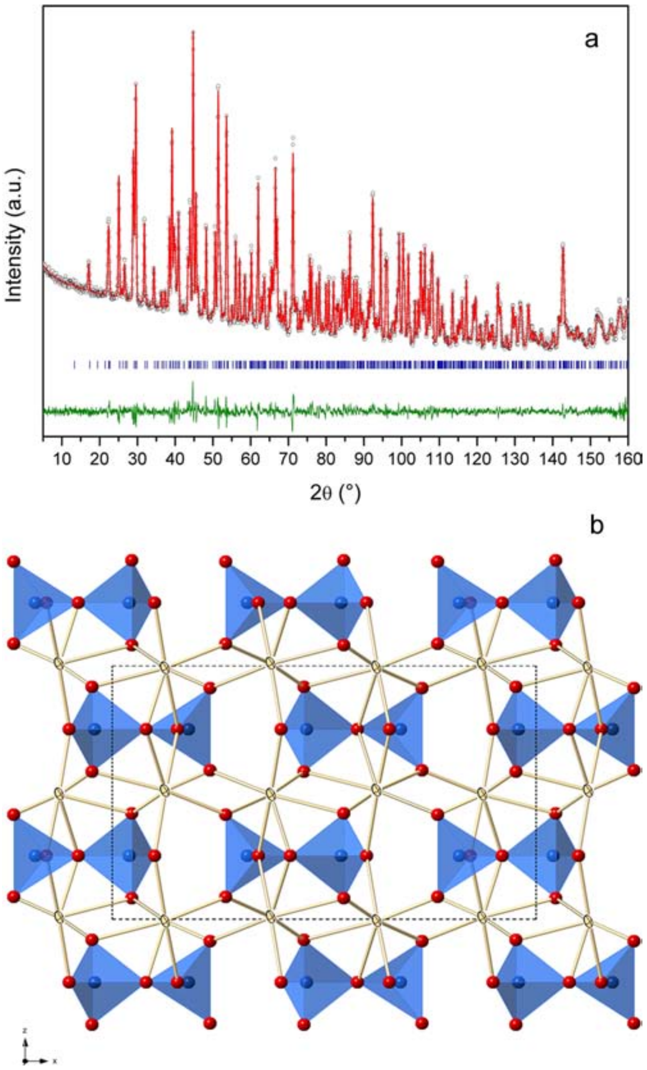

Figure 5. (a) Experimental (circles) and fitted (solid line) neutron diffraction pattern (λ 1.594 Å) of δ-$La_{0.2}Ho_{1.8}Si_2O_7$ (LaHo90). The difference curve is also shown. The indexing corresponds to the δ phase. (b) View of the δ-$La_{0.2}Ho_{1.8}Si_2O_7$ refined structure along the [010] direction. The thermal ellipsoids correspond to the unique RE site and have been drawn with a 99% probability presence.

Table 5. Main Atomic Distances and Angles for δ-$La_{0.2}Ho_{1.8}Si_2O_7$ (LaHo90) Calcined at 1600 °C

La/Ho–O distance (Å)		Si1–O distance (Å)		Si2–O distance (Å)	
La/Ho–O1	2.238(2)	Si1–O1	1.606 (3)	Si2–O3	1.681(4)
La/Ho–O1	2.384(2)	Si1–O1	1.606 (3)	Si2–O4	1.617(2)
La/Ho–O2	2.327(2)	Si1–O2	1.606 (4)	Si2–O4	1.617(2)
La/Ho–O3	2.512(2)	Si1–O3	1.659(4)	Si2–O5	1.606(4)
La/Ho–O4	2.466(2)				
La/Ho–O4	2.284(2)				
La/Ho–O5	2.345(2)				
		Si–O Angles (deg)			
O1–Si1–O1	112.7(2)		O3–Si2–O4	98.9(2)	
O1–Si1–O2	115.1(1)		O3–Si2–O4	98.9(2)	
O1–Si1–O3	100.2(2)		O3–Si2–O5	110.2(2)	
O1–Si1–O2	115.1(1)		O4–Si2–O4	116.5(2)	
O1–Si1–O3	100.2(2)		O4–Si2–O5	114.8(1)	
O2–Si1–O3	111.4(2)		O4–Si2–O5	114.8(1)	

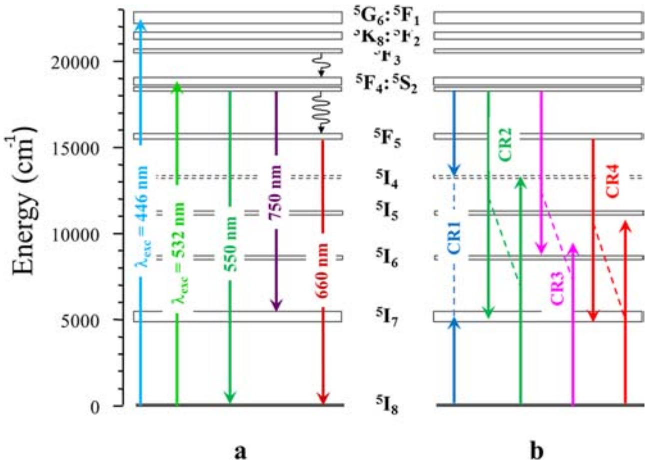

Figure 6. (a) Energy level diagram of Ho^{3+}:$La_2Si_2O_7$ showing the relevant luminescent emissions. Under 446 nm (continuous wave) or 532 nm (pulsed) excitations, the $^5F_4$:$^5S_2$ and $^5F_5$ multiplets are populated, giving rise to emissions in the 550–800 nm wavelength range, as shown in the diagram. (b) Possible cross-relaxation schemes affecting the green and red emitting levels.

The emission spectrum of the 2.5% Ho-doped G-$La_2Si_2O_7$ sample excited at 446 nm is presented in Figure 7b. Three characteristic emission bands in the 500–800 nm region are observed, which are responsible for the strong green luminescence of the sample (inset of Figure 7b), which shows CIE coordinates $x = 0.29$ and $y = 0.69$. The dominant yellow-green emission in the 525–560 nm region of the spectrum is attributed to the transition from the thermalized $^5F_4$:$^5S_2$ states of Ho^{3+} to the $^5I_8$ ground state, while the red emission (630–670 nm) corresponds to the $^5F_5 \rightarrow {}^5I_8$ transition and the 740–770 nm band is associated with the $^5F_4$:$^5S_2 \rightarrow {}^5I_7$ transition.

Table 4. Refined Atomic Coordinates for δ-$La_{0.2}Ho_{1.8}Si_2O_7$ (LaHo90) Calcined at 1600 °C from Neutron Powder Diffraction Data Collected at Room Temperature[a]

atom	site	*x*	*y*	*z*	U_{iso} (×100) ($Å^2$)	occ
La/Ho	8d	0.12585(8)	0.3378(2)	−0.0080(2)	0.26(2)	0.1/0.9
Si1	4c	0.3198(2)	0.3765(6)	0.25	0.57(7)	1
Si2	4c	0.5403(2)	0.6227(6)	0.25	0.52(6)	1
O1	8d	0.2686(1)	0.4847(3)	0.0872(2)	0.82(4)	1
O2	4c	0.3447(2)	0.0648(5)	0.25	0.89(6)	1
O3	4c	0.4202(2)	0.5596(5)	0.25	0.61(5)	1
O4	8d	0.5470(1)	0.7909(4)	0.0826(2)	0.98(4)	1
O5	4c	0.6005(2)	0.3493(5)	0.25	0.97(5)	1

[a] Crystal data: space group *Pnam*, $a = 13.7482(4)$ Å, $b = 5.0316(1)$ Å, $c = 8.2123(3)$ Å, $R_{wp} = 3.05\%$, $R_p = 2.39\%$, $\chi^2 = 1.64$.

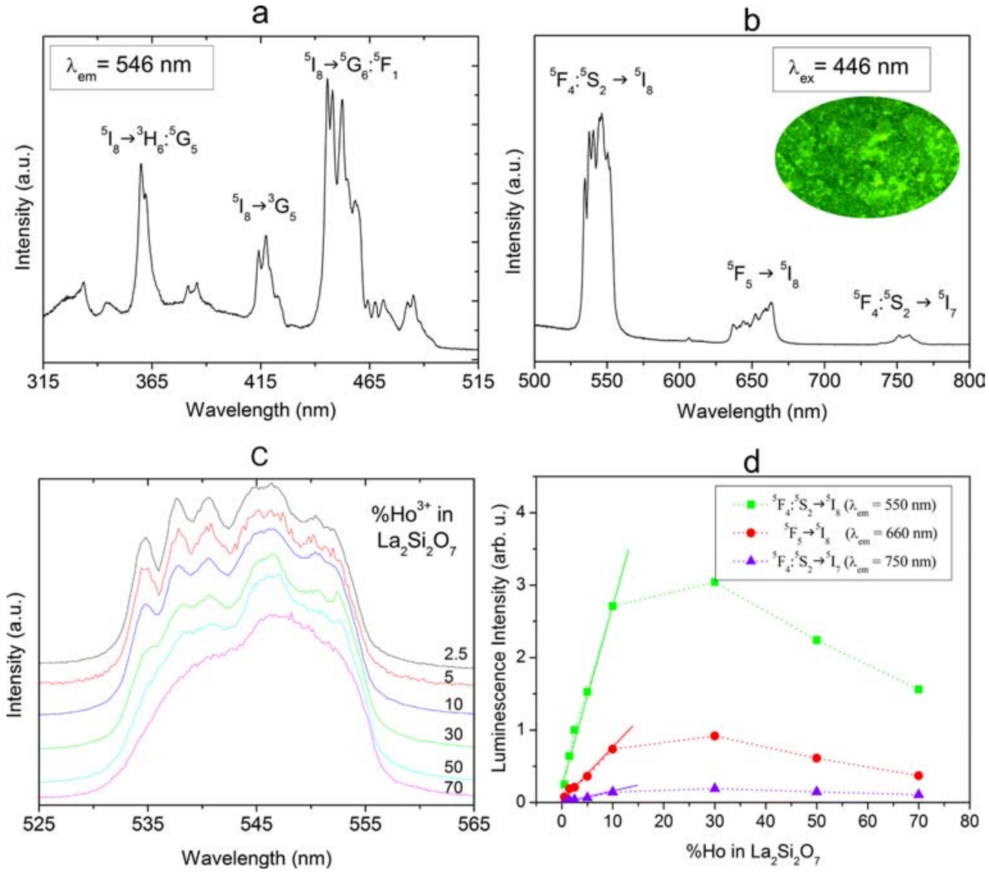

Figure 7. Excitation (a) and emission (b) spectra of the 2.5% Ho-doped G-$La_2Si_2O_7$ phosphor. Inset: photograph of LaHo2.5 powder taken under 455 nm illumination. (c) The 525−565 nm region of the emission spectra of the different Ho-doped G-$La_2Si_2O_7$ phosphors. (d) Linear increase of luminescence intensity of all visible emissions with Ho content up to [Ho] ≈ 10 mol %, (at higher concentrations this proportionality is lost and all emissions show concentration quenching effects).

The rest of the compositions showed emission spectra very similar to that of the 2.5% Ho sample, but a progressive loss of resolution of the emission lines was observed with increasing Ho content (Figure 7c). This fact could be explained on the basis of the ASD results, which indicated the presence of Ho in a unique crystallographic site at low Ho content, while a second site was occupied as the Ho content increased above ∼50%. On the other hand, the luminescence intensities of all visible emissions increase linearly with Ho content up to [Ho] ≈ 10 mol % (Figure 7d), while for higher concentrations this proportionality is lost and the emissions show concentration quenching effects. In order to understand the origin of such concentration quenching, the luminescence dynamics under pulsed excitation has been investigated.

For that purpose the luminescence of Ho^{3+} ions has been obtained under pulsed excitation using the second harmonics of a Nd:YAG laser at λ_{exc} 532 nm. Under this excitation, the $^5F_4:^5S_2$ multiplet is directly populated (see Figure 6a) and the emission spectra are coincident with those shown in Figure 7b. The lifetimes of the $^5F_4:^5S_2$ levels have been obtained by monitoring the green (550 nm) luminescence, corresponding to the $^5F_4:^5S_2 \rightarrow {}^5I_8$ transition. The luminescence decays are presented in Figure 8a, for samples with variable Ho concentration, from LaHo0.5 to LaHo70. The decays exhibit single exponential behavior, $I_G = I_{G,0}\exp(-t/\tau_G)$, and the characteristic lifetime values (τ_G) have been obtained from the least-squares fitting of the experimental data. The corresponding theoretical decays are also included in Figure 8a (solid lines). The calculated lifetime is $\tau_G = 0.22$ μs, independent of Ho concentration in the range 0.5% < [Ho] < 10%. Above this concentration the lifetime decreases sharply (Table 6 and Figure 9) and reaches the value $\tau_G = 0.045$ μs at [Ho] = 70%. It has been verified that the same lifetime values are obtained with monitoring at λ_{em} ∼750 nm, corresponding to the $^5F_4:^5S_2 \rightarrow {}^5I_7$ transition, which originates from the same emitting multiplet.

The second emission of Ho^{3+} ions in the visible range appears in the red spectral region at λ ∼660 nm, and it can be associated with the $^5F_5 \rightarrow {}^5I_8$ transition. The luminescence decays, for different dopant contents, are presented in Figure 8b. As is illustrated, the luminescence temporal evolution reveals an initial rise, reaching a maximum value and then an exponential decay. The observed rise is related to the fact that the emitting $^5F_5$ multiplet becomes populated from the upper levels and therefore its filling is expected to follow the dynamics of the green-emitting $^5F_4:^5S_2$ multiplet (see Figure 6a).

According to this scheme the overall temporal evolution can be described by a double-exponential dependence given by

$$I_R = I_{R,0}(\exp(-t/\tau_R) - \exp(-t/\tau_{rise})) \qquad (1)$$

where τ_R is the characteristic lifetime of the $^5F_5$ multiplet while τ_{rise} describes the initial rise of the red emission. This last time constant, describing the initial filling of the $^5F_5$ multiplet from the upper levels, is expected to be coincident with the lifetime of the $^5F_4:^5S_2$ multiplet (τ_G) (see the Supporting Information for a further description of the de-excitation dynamics of Ho^{3+} ions).

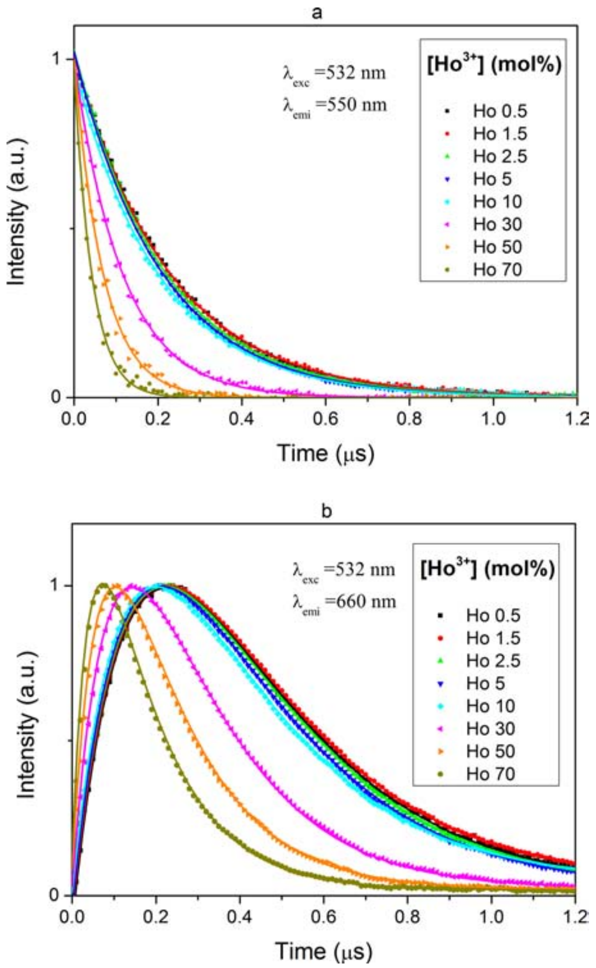

Figure 8. Decay of the 550 nm (a) and 660 nm (b) emissions of Ho^{3+}:$La_2Si_2O_7$ for different dopant concentrations, after 532 nm pulsed excitation. The symbols correspond to the experimental data and the lines to the fitting to a single- (a) and double-exponential (b) dependence.

Table 6. Calculated Characteristic Lifetimes of the Visible Luminescence Emissions of Ho^{3+} Ions for Different RE Contents

		$^5F_5 \rightarrow {}^5I_8$ (λ_{em} 660 nm)	
[Ho] (mol %)	$^5F_4$:$^5S_2 \rightarrow {}^5I_8$ (λ_{em} 550 nm) t_G (μs)	t_{rise} (μs)	t_R (μs)
0.5	0.22	0.21	0.22
1.5	0.22	0.21	0.22
2.5	0.21	0.21	0.22
5	0.20	0.20	0.21
10	0.19	0.19	0.20
30	0.12	0.12	0.18
50	0.070	0.072	0.16
70	0.045	0.045	0.14

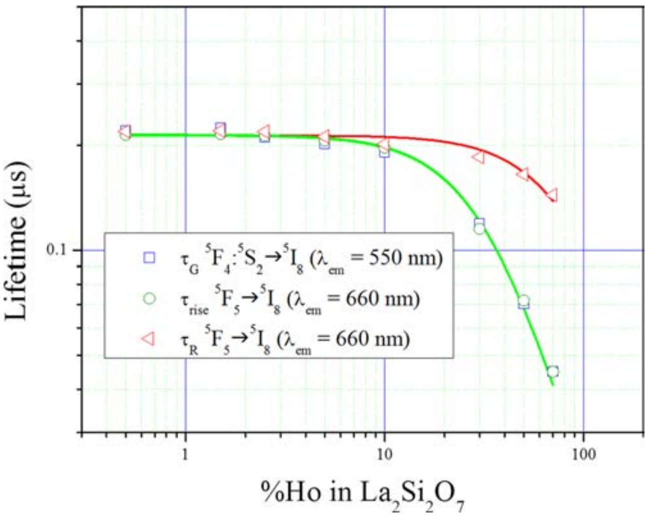

Figure 9. Concentration dependence of the characteristic time constants of Ho^{3+} luminescence decays. The rise time of the 660 nm emission is always coincident with the decay of the 550 nm emission. The lifetimes are basically constant up to [Ho] < 10%, and above this value they are reduced when the Ho concentration increases, the emission from the $^5F_4$:$^5S_2$ multiplets being more sensitive than that of the $^5F_5$ multiplet. Continuous lines represent the least-squares fitting of the experimental data to eq 4. The best fitting corresponds to $S = 6$, which is a dipole−dipole coupling between interacting Ho^{3+} ions.

The experimental decays have been fitted to eq 1 by using a least-squares algorithm and calculating simultaneously both characteristic time constants (τ_{rise} and τ_R). The calculated parameters are summarized in Table 6, and the theoretical decays are included as solid lines in Figure 8b. As can be observed, the time at which the luminescence pulse has its maximum intensity changes with Ho concentration, appearing at shorter times when the Ho concentration increases. This fact is due to the shortening of the $^5F_4$:$^5S_2$ multiplet's lifetime, as described above, and it is predicted from the temporal evolution given in eq 1. The characteristic lifetimes of the green- and red-emitting levels for different Ho^{3+} concentrations, as well as the rise time calculated from the experimental fitting of Figure 8b, are included in Table 6 and represented in Figure 9 as a function of Ho concentration. It can be observed that, indeed, the rise time values of the red emission (circles) are coincident with the $^5F_4$:$^5S_2$ lifetimes (squares).

These lifetimes are independent of Ho concentrations up to [Ho] ≈ 10% and then become progressively shorter as the concentration increases, this decrease being more pronounced for the green emission than for the red emission. The lifetime reduction is possibly related to cross-relaxation (CR) processes between Ho^{3+} ions, leading to concentration quenching. Such phenomena have been observed in many Ho^{3+}-doped materials, and several cross-relaxation mechanisms involving Ho^{3+} excited state levels have been proposed in the literature.[41−50] It is worth mentioning that in some materials with a high Ho content, such as $HoLiF_4$,[41] concentration quenching can be so severe as to fully suppress some of the luminescent emissions (including the 550 nm emission).

The most plausible cross-relaxation schemes affecting the green and red emitting levels (indicated in Figure 6b) are as follows.

For the 550 nm emission

CR1: ($^5F_4$:$^5S_2$, $^5I_8$) → ($^5I_4$, $^5I_7$) refs 42, 43, 45, 46, 48, 49
CR2: ($^5F_4$:$^5S_2$, $^5I_8$) → ($^5I_7$, $^5I_4$) refs 48, 49
CR3: ($^5F_4$:$^5S_2$, $^5I_8$) → ($^5I_6$, $^5I_6$) refs 41, 42, 49

For the 660 nm emission

CR4: ($^5F_5$, $^5I_8$) → ($^5I_7$, $^5I_5$) ref 48

In the present case, it has been shown in Figure 9 that both green and red emissions exhibit lifetime reduction for a doping concentration above [Ho^{3+}] ≈ 10%, although the decrease is more pronounced for the green than for the red emission. This suggests that cross relaxation from the $^5F_5$ multiplet is less efficient than that from the upper $^5F_4$:$^5S_2$ levels. This is consistent with the fact that these last multiplets are potentially affected by several cross-relaxation paths (CR1−CR3), while the $^5F_5$ multiplet seems to be affected by a single process (CR4). The fact that several CR processes are possibly involved in Ho concentration quenching makes difficult a detailed description of this phenomenon. Nevertheless, it is possible to make some quantitative estimation of its efficiency and concentration dependence, always bearing in mind that such a description will be a phenomenological average of all the possible CR schemes involved.

Cross relaxation, as does any other energy transfer process, reduces the lifetime in comparison to the value observed for low concentration (noninteracting ions). Its probability will depend on dopant concentration and on the multipolar order of the ion−ion interaction.[51,52] Its calculation will depend also on the possibility of energy migration between excited donors (diffusion) and its probability compared to that of transfer to the acceptors.[53−56] Considering a sufficiently fast diffusion between donor ions, luminescence decays follow a single-exponential dependence (in agreement with our experimental observations) and the lifetime is given by[55,57,58]

$$\frac{1}{\tau_{\mathrm{exp}}} = \frac{1}{\tau_0} + W_{\mathrm{ET}}^{(S)} N_{\mathrm{A}} \tag{2}$$

where τ_{exp} is the experimental lifetime for an acceptor concentration N_A, while τ_0 represents the intrinsic lifetime in the absence of energy transfer, i.e. at low dopant concentration, while the transfer rate, $W_{\mathrm{ET}}^{(S)}$, depends on donor concentration N_D as

$$W_{\mathrm{ET}}^{(S)} = V \times N_{\mathrm{D}}^{((S-3)/3)} \tag{3}$$

where V depends on the microparameters of energy transfer and the multipolar order of interaction, S (S = 6, 8, 10 for dipole−dipole, dipole−quadrupole, and quadrupole−quadrupole, respectively).

For cross relaxation, where donors and acceptors are the same rare-earth ions ($N_A = N_D$ = [Ho]), the concentration dependence of the decay time can finally be summarized as

$$\tau_{\mathrm{exp}} = \frac{\tau_0}{1 + V \times \tau_0 \times [\mathrm{Ho}]^{S/3}} \tag{4}$$

From the observed concentration dependence of the green and red emissions (Figure 9), a least-squares fitting to eq 4 indicates that the best fitting corresponds to S = 6, which is a dipole−dipole coupling mechanism between interacting Ho^{3+} ions. The calculated concentration dependences for both green and red emissions have been included (continuous lines) in the figure. The calculated coupling parameters V, for both emissions, are given in Table 7. It can be observed that the calculated V value for the red emission is 1 order of magnitude smaller than that for the green emission, consistent with the lower quenching of the former.

Table 7. Fitting Parameters of the Concentration Dependence of Ho^{3+} Lifetimes (Eq 4)[a]

	V (cm^6 s^{-1})	τ_0 (μs)	N_C (mol %)	R_C (Å)
$^5F_4$:$^5S_2$ → $^5I_8$ (λ_{em} 550 nm)	2.5×10^{-37}	0.22	34	6.1
$^5F_5$ → $^5I_8$ (λ_{em} 660 nm)	3.2×10^{-38}	0.21	95	4.4

[a] 1 mol % = 1.28×10^{20} ions/cm^3.

An alternative description would rely on the dependence of concentration quenching with the distance between interacting ions. It is usually expressed defining a "critical doping concentration" (N_C), for which the probability of cross relaxation equals that of intrinsic de-excitation and which, from eq 4, is given by $N_C = (V\tau_0)^{-1/2}$, and then a "critical distance" ($R_C \approx (N_C)^{1/3}$) for cross relaxation can be obtained. The corresponding values are also given in Table 7.

When these values are compared with the nearest-neighbor distance between lanthanide ions in G-$La_2Si_2O_7$ (~4 Å), it can be observed that the critical distance for cross relaxation affecting the red emission would be reached only for nearest-neighbor occupancy between interacting ions and then becomes operative only at very high Ho concentrations. Cross relaxation affecting the green emission would be operative for Ho ions at higher separations and therefore at some lower dopant levels; this is consistent again with the observed data presented in Figure 9.

In comparison to other Ho-doped hosts, the lifetime values reported in the literature for the visible Ho emissions vary among wide limits, from tens of microseconds to tens of nanoseconds, depending on the host. This variation can be understood by considering the energy level scheme of Ho^{3+} ions (see Figure 6) with a number of electronic levels filling the gap from the ground state to the emitting upper levels. This energy ladder implies that the role of nonradiative (multiphonon) transitions between the different multiplets becomes extremely important, with its probability increasing with the phonon energy of the host.[59] Consequently, low-phonon materials exhibit generally long lifetimes, while increasing the phonon energy of the material reduces lifetime values. For instance, for YLF ($E_{ph} \approx 566$ cm^{-1}) the lifetime reported for the $^5F_5$ multiplet is 57 μs, while it is reduced to 9 μs for LNB ($E_{ph} \approx 880$ cm^{-1}) and 57 ns for borate crystals ($E_{ph} \approx 1400$ cm^{-1}).[58,60−62] Considering the relatively high-phonon energies of silicate materials ($E_{ph} \approx 1100$ cm^{-1}), the measured lifetimes, and their concentration dependences, are consistent with the observed variations between different hosts.

■ CONCLUSIONS

The $La_2Si_2O_7$−$Ho_2Si_2O_7$ system annealed at 1600 °C shows a solid solubility region of G-$(La,Ho)_2Si_2O_7$ which extends to the $La_{0.6}Ho_{1.4}Si_2O_7$ composition ,while δ-$(La,Ho)_2Si_2O_7$ is the stable phase for Ho contents higher than 90% ($La_{0.2}Ho_{1.8}Si_2O_7$). Intermediate compositions show a two-phase domain (G+δ), where the G/δ ratio decreases with increasing Ho content while the La/Ho ratio is kept fixed for each phase. Unexpectedly, the phase boundaries appear at different compositional values in comparison to the $(La,Y)_2Si_2O_7$ system, which indicates that factors other than purely the ionic radii influence the phase stability of binary disilicate systems. Anomalous diffraction data interestingly indicated that the La for Ho substitution mechanism in the G-$(La,Ho)_2Si_2O_7$ polymorph is not homogeneous; rather, a preferential occupation of Ho for the RE2 site is observed. Another remarkable aspect of the structural analysis of this system is the confirmation of space group *Pnma* for the δ phase, as evidenced from neutron powder diffraction data. Finally, it has been demonstrated that, in spite of the high phonon energy characteristic of silicates, Ho^{3+} ions exhibit their typical luminescence in the 500−800 nm range, arising from the excited $^5F_4$:$^5S_2$ and $^5F_5$ multiplets. The lifetimes remain unchanged with Ho concentration in the range 0.5% < [Ho^{3+}] < 10%, and only above this value does concentration quenching become operative with the corresponding lifetime reduction. The observed concentration dependence of the visible emissions' lifetimes can be explained by considering a dipole−dipole coupling between interacting Ho^{3+} ions. The calculated critical distance for cross relaxation affecting the red emission ($R_C \approx 4.4$ Å) would be reached only for nearest-neighbor occupancy between interacting ions and then becomes operative only at very high Ho concentrations. Cross relaxation affecting the green emission would be operative for Ho ions at higher separations ($R_C \approx 6.1$ Å) and therefore becomes operative at some lower dopant levels.

■ ASSOCIATED CONTENT

Ⓢ Supporting Information

Text giving rate equations describing the de-excitation dynamics of Ho^{3+} ions after 532 nm pulsed excitation and CIF files giving crystal data for G-$La_{1.0}Ho_{1.0}Si_2O_7$ and δ-$La_{0.2}Ho_{1.8}Si_2O_7$. This material is available free of charge via the Internet at http://pubs.acs.org.

■ AUTHOR INFORMATION

Corresponding Author

*A.I.B.: e-mail, anieto@icmse.csic.es; tel, +34 954489545; fax, +34 954460665.

Notes

The authors declare no competing financial interest.

■ ACKNOWLEDGMENTS

A.J.F.-C. gratefully acknowledges an FPDI grant from the Junta de Andalucía and J.G-S. an FPI grant from the MICINN. This work was supported by the DGICYT (Project No. CTQ2010-14874/BQU), MEC (Project No. MAT2012-34919), and Junta de Andalucía (JA FQM 06090). M.A. thanks the ANR for its financial support of the project CrystOG ANR-12-JS08-0002-01. We thank the ESRF for provision of time on beamline ID31. I.L.L. is acknowledged for beamtime.

■ REFERENCES

(1) Felsche, J. *Struct. Bonding (Berlin)* **1973**, *13*, 99−197.

(2) Shannon, R. D. *Acta Crystallogr., Sect. A* **1976**, *32*, 751.

(3) Dolan, M. D.; Harlan, B.; White, J. S.; Hall, M.; Misture, S. T.; Bancheri, S. C.; Bewlay, B. *Powder Diffr.* **2008**, *23*, 20−25.

(4) Redhammer, G. J.; Roth, G. *Acta Crystallogr., Sect. C* **2003**, *59*, i103−i106.

(5) Christensen, A. N. *Acta Chem. Scand.* **1997**, *51*, 37−43.

(6) Christensen, A. N. *Z. Kristallogr.* **1994**, *209*, 7−13.

(7) Ito, I.; Johnson, H. *Am. Mineral.* **1968**, *53*, 1940−1952.

(8) Allix, M.; Alba, M. D.; Florian, P.; Fernández-Carrión, A. J.; Suchomel, M. R.; Escudero, A.; Suard, E.; Becerro, A. I. *J. Appl. Crystallogr.* **2011**, *44*, 846−852.

(9) Fernández-Carrión, A. J.; Alba, M. D.; Escudero, A.; Becerro, A. I. *J. Solid State Chem.* **2011**, *184*, 1882−1889.

(10) Fernández-Carrión, A. J.; Escudero, A.; Suchomel, M.; Becerro, A. I. *J. Eur. Ceram. Soc.* **2012**, *32*, 2477−2486.

(11) Becerro, A. I.; Escudero, A. *Chem. Mater.* **2005**, *17*, 112−117.

(12) Becerro, A. I.; Escudero, A. *J. Solid State Chem.* **2005**, *178*, 1−7.

(13) Fernández-Carrión, A. J.; Allix, M.; Florian, P.; Suchomel, M. R.; Becerro, A. I. *J. Phys. Chem. C* **2012**, *116*, 21523−21535.

(14) Pomeroy, M. J.; Nestor, E.; Ramesh, R.; Hampshire, S. *J. Am. Ceram. Soc.* **2005**, *88*, 875−881.

(15) Maier, N.; Nickel, K. G.; Rixecker, G. *J. Eur. Ceram. Soc.* **2007**, *27*, 2705−2713.

(16) Meiss, D.; Wischert, W.; Kemmler-Sack, S. *Phys. Status Solidi A* **1992**, *134*, 539−546.

(17) Nikl, M.; Begnamini, A. M.; Jary, V.; Niznansky, D.; Mihokova, E. *Phys. Status Solidi RRL* **2009**, *9*, 293−295.

(18) Zhang, Z.; Wang, Y.; Zhang, F.; Cao, H. *J. Alloys Compd.* **2011**, *509*, 5023−5027.

(19) Díaz, M.; Pecharromán, C.; del Monte, F.; Sanz, J.; Iglesias, J. E.; Moya, J. S.; Yamagata, C.; Mello-Castanho, S. *Chem. Mater.* **2005**, *17*, 1774−1782.

(20) Sokolnicki, J. *Mater. Chem. Phys.* **2011**, *131*, 306−312.

(21) Sokolnicki, J. *J. Lumin.* **2013**, *134*, 600−606.

(22) Feng, H.; Ding, D.; Li, H.; Lu, S.; Pan, S.; Chen, X.; Ren, G. *J. Alloys Compd.* **2010**, *489*, 645−649.

(23) Zhou, P.; Yu, X.; Yang, L.; Yang, S.; Gao, W. *J. Lumin.* **2007**, *124*, 241−244.

(24) Hreniak, D.; Strek, W.; Opalinska, A.; Nyk, M.; Wolcyrz, M.; Lojkowski, W.; Misiewicz, J. *J. Sol-Gel Sci. Tech* **2004**, *32*, 195−200.

(25) Li, Y.; Wei, X.; Yin, M.; Tao, Y. *Opt. Mater.* **2011**, *33*, 1239−1242.

(26) Gerasimov, I.; Sidletsky, O.; Neicheva, S.; Grinyov, B.; Baumer, V.; Galenin, E.; Katrunov, K.; Tkchenko, S.; Voloshina, O.; Zhukov, A. *J. Cryst. Growth* **2011**, *318*, 805−808.

(27) Baumer, V.; Gerasimov, I.; Sidletsky, O.; Voloshina, O.; Neicheva, S. *J. Alloys Compd.* **2011**, *509*, 8478−8482.

(28) Mihóková, E.; Fasoli, M.; Moretti, F.; Nikl, M.; Jarý, V.; Ren, G.; Vedda, A. *Opt. Mater.* **2012**, *34*, 872−877.

(29) Sokolnicki, J. *J. Phys. Condens. Mater.* **2010**, *22*, 275301.

(30) Sokolnicki, J.; Guzik, M. *Opt. Mater.* **2009**, *31*, 826−830.

(31) Diamente, P. R.; Raudsepp, M.; van Veggel, C. J. M. *Adv. Funct. Mater.* **2007**, *17*, 363−368.

(32) Piriou, B.; Richard-Poulet, M.; Parmentier, J.; Ferey, F.; Vilminot, S. *J. Alloys Compd.* **1997**, *262−263*, 450−453.

(33) Boyer, J. C.; Vetrone, F.; Capobianco, J. A. *J. Appl. Phys.* **2003**, *93*, 9460−9465.

(34) *ICDD PDF-4+ 2011*; Kabekkodu, S., Ed.; International Centre for Diffraction Data, Newtown Square, PA, USA, 2011.

(35) Rietveld, H. M. *J. Appl. Crystallogr.* **1969**, *2*, 65−71.

(36) Petricek, V.; Dusek, M.; Palatinus, L. *JANA2006 Software*; Institute of Physics, Academy of Sciences of the Czech Republic, Praha, Czech Republic, 2006; http://www-xray.fzu.cz/jana/jana.html.

(37) Wright, J. P.; Vaughan, G. B. M.; Fitch, A. N. *IUCr Computing Commission Newsletter* **2003**, *1*, 92−94.

(38) Smolin, Y. J.; Shepelev, Y. F. *Acta Crystallogr.* **1970**, *26B*, 484−492.

(39) Dias, H. W.; Glasser, F. P.; Gunwardane, R. P.; Howie, R. A. *Z. Kristallogr.* **1990**, *191*, 117−123.

(40) Becerro, A. I.; Escudero, A.; Florian, P.; Massiot, D.; Alba, M. D. *J. Solid State Chem.* **2004**, *177*, 2783−2789.

(41) Courrol, L. C.; Gomes, L.; Morato, S. P. *Phys. Rev. B* **1995**, *51*, 3344−3352.

(42) Gomes, L.; Courrol, L. C.; Tarelho, V. G.; Ranieri, I. M. *Phys. Rev. B* **1996**, *54*, 3825−3829.

(43) Malinowski, M.; Piramidowicz, R.; Frukacz, Z.; Chadeyron, G.; Mahiou, R.; Joubert, M. F. *Opt. Mater.* **1999**, *12*, 409−423.

(44) Kück, S.; Sokólska, I. *Chem. Phys. Lett.* **2000**, *325*, 257−263.

(45) Ebendorff-Heidepriem, H.; Szabó, I.; Rasztovits, Z. E. . *Opt. Mater.* **2000**, *14*, 127−136.

(46) Osiac, E.; Sokólska, I.; Kück, S. *Phys. Rev. B* **2002**, *65*, 235119.

(47) Capobianco, J. A.; Boyer, J. C.; Vetrone, F.; Speghini, A.; Bettinelli, M. *Chem. Mater.* **2002**, *14*, 2915−2921.

(48) Silver, J.; Barrett, E.; Marsh, P. J.; Withnall, R. *J. Phys. Chem. B* **2003**, *107*, 9236−9242.

(49) Karmakar, B. *J. Solid State Chem.* **2005**, *178*, 2663−2672.

(50) Lavin, V.; Lahoz, F.; Martín, I. R.; Rodríguez-Mendoza, U. R.; Cáceres, J. M. *Opt. Mater.* **2005**, *27*, 1754−1761.

(51) Förster, Th. *Ann. Phys.* **1948**, *2*, 55−75.

(52) Dexter, D. L. *J. Chem. Phys.* **1953**, *21*, 836−850.

(53) Inokuti, M.; Hirayama, F. *J. Chem. Phys.* **1965**, *43*, 1978−1989.

(54) Yokota, M.; Tanimoto, O. *J. Phys. Soc. Jpn.* **1967**, *22*, 779−784.

(55) Burshtein, A. I. *Sov. Phys. JETP* **1972**, *35*, 882−5.

(56) Martín, I. R.; Rodríguez, V. D.; Rodríguez-Mendoza, U. R.; Lavín, V.; Montoya, E.; Jaque, D. *J. Chem. Phys.* **1999**, *111*, 1191−1194.

(57) De Sousa, D. F.; Nunes, L. A. O. *Phys. Rev. B* **2002**, *66*, 024027−7.

(58) Van Uitert, L. G. *J. Electrochem. Soc.* **1967**, *114*, 1048−1053.

(59) Reisfeld, R. In *Spectroscopy of Solid-State Laser-Type Materials*; di Bartolo, B., Ed.; Plenum Press: New York, 1987; EttoreMajorana International Science Series.

(60) Wnuk, A.; Kaczkan, M.; Frukacz, Z.; Pracka, I.; Chadeyron, G.; Joubert, M.-F.; Malinowski, M. *J. Alloys Compd.* **2002**, *341*, 353−357.

(61) Lorenzo, A.; Bausá, L. E.; Sanz-García, J. A.; García-Solé, J. *J. Phys. Condens. Matter* **1996**, *8*, 5781−5792.

(62) Wei, Q.; Li, X.; Song, M.; Wang, Z.; Wang, G.; Long, X. *Opt. Mater.* **2008**, *30*, 1495−1498.